

A Technique for Rotation Vector Position Determination for Tumbling Rocket Bodies

Laurence D. J. Blacketer¹, Hugh G. Lewis², Hodei Urrutxua³

¹Astronautics Research Group, The University of Southampton, Southampton SO17 1BJ, UK. ldjb1g15@soton.ac.uk

²Astronautics Research Group, The University of Southampton, Southampton SO17 1BJ, UK. h.g.lewis@soton.ac.uk

³Universidad Rey Juan Carlos, Calle Tulipán, s/n, 28933 Móstoles, Madrid, Spain. hodei.urrutxua@urjc.es

ABSTRACT

Knowledge of space object attitude state is useful for a range of applications, from accurate modelling of attitude-dependent forces such as solar radiation pressure and atmospheric drag, to planning missions that require interfacing with uncontrolled space objects, such as Active Debris Removal. In this paper a technique is examined for determining the position of the rotation vector of a tumbling low-Earth orbit rocket body by fitting a synthetic light curve to a real light curve. The technique was first tested on synthetic light curves, for which the values of all inputs were known. The synthetic light curves were generated by applying a Cook-Torrence Bidirectional Reflectance Distribution Function to a faceted object geometry. The technique was then tested on a real light curve of a Long March 2D rocket body. The results show a similar rotation vector determination performance on either real or synthetic light curve data. As only a very simple representation of the rocket body geometry was used, these initial results indicate that precise modelling of object geometry is not required. However further testing is needed confirm the findings of this paper and to examine the applicability to a wider range of rocket bodies.

1 INTRODUCTION

Knowledge of space object attitude state can be useful for a wide range of applications. One example is calculation of attitude dependent forces such as Solar Radiation Pressure (SRP), atmospheric torques and atmospheric drag. Depending on the orbital regime, these forces can have a substantial effect on the future position of space objects. Therefore the highest accuracy predictions of the future position of a space object requires information on attitude state. The higher accuracy positioning data, made possible by improved attitude state information, is an important component of ongoing efforts to improve our Space Situational Awareness (SSA) capabilities.

Simulations of future debris populations have suggested that the targeted removal of high risk objects may be required to prevent a growth in the debris population [1]. This is known as Active Debris Removal (ADR). Typical ADR proposals involve a rendezvous with the target object, followed by a capture technique such as a robotic arm, net or harpoon. As the most likely ADR targets are large massive objects, prior knowledge of the attitude state would be required both to find objects within the capabilities of a particular mission and for planning the capture phase of the mission. Any other mission that requires interfacing with an uncontrolled object would have similar requirements, such as on-orbit servicing or End-of-Life (EOL) de-orbiting services.

In the past, optical light curves have been used to determine properties of asteroids. In those applications light curves have been used to determine object shape, rotation axis position and reflection characteristics such as albedo [2, 3]. This is typically done with a priori information or assumptions, i.e. determining shape with known attitude, or determining attitude with known shape. Building upon this heritage, light curve analysis has also been applied to space objects to determine similar properties [4, 5, 6].

Optical light curves provide a further advantage over other observation techniques such as radar, in that large numbers of light curves can be collected using relatively simple, low-cost, hardware. For this reason, light curves may not only be useful for targeted observations of particular objects, but could provide large amounts of data to an SSA architecture autonomously.

This paper examines a technique for determining the position of the rotation vector for a tumbling object. The objects under consideration are rocket bodies This allows for assumptions to be made on the object shape and attitude motion. The rotation vector position was determined by generating a match between a real target light curve and a synthetic

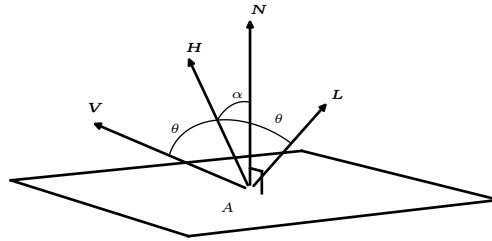


Fig. 1. The reflection geometry. **V** is the observation vector, **L** is the illumination vector and **H** is the angular bisector of these two vectors. **N** is the surface normal and *A* is the surface area.

light curve for which the rotation vector position was known. In order for the synthetic light curve to be the correct solution, it must be the only rotation vector position for which a match can be generated. The effectiveness of this technique was first evaluated on four synthetic target light curves, for which all inputs were known. Then, the technique was applied to a real target light curve. By comparing the results for the real light curve to those of the synthetic light curves, the sensitivity of this technique to errors in the inputs was assessed.

2 METHODOLOGY

Brightness Model

To generate a synthetic light curve, a model is required for calculating the reflected flux from a collection of surfaces. This can be achieved by using a function that describes the distribution of reflected flux as a function of viewing conditions and the optical properties of the surfaces. Such a function is called a Bidirectional Reflectance Distribution Function (BRDF). By applying a BRDF to faceted geometry of a space object, and summing the brightness contributions of each illuminated and observable facet, a synthetic light curve can be generated.

The BRDF employed in this paper is the Cook Torrance BRDF, which is given by

$$B_i = (sR_s + dR_d)\pi A_i(\mathbf{N}_i \cdot \mathbf{L})(\mathbf{N}_i \cdot \mathbf{V}), \tag{1}$$

where B_i is the ratio of incident to reflected flux at the i^{th} facet, A_i is the area of the i^{th} facet, R_s and R_d are the specular and diffuse bidirectional reflectances and s and d are the specular and diffuse coefficients, with $s + d = 1$. The surface normal vector, **N**, illumination vector, **L**, and the observation vector, **V**, are shown in Fig 1.

The diffuse reflectance is given by the equation

$$R_d = \frac{\omega}{\pi}, \tag{2}$$

with ω being the diffuse albedo of the surface. The specular reflectance is

$$R_s = \frac{F}{\pi} \frac{DG}{(\mathbf{N} \cdot \mathbf{L})(\mathbf{N} \cdot \mathbf{V})}, \tag{3}$$

where F is the surface reflectance, G is a geometric attenuation factor and D is the facet slope function. Calculation of the surface reflectance, F , requires a value for the reflectance at normal incidence, F_0 . Using a simplification from [4], F_0 , is taken to be equal to the diffuse albedo, ω . The geometric attenuation factor G , which accounts for the masking and shadowing of facets by one another, is calculated using only the vectors **N**, **V** and **L**. The facet slope function D provides the fraction of facets which are aligned with the angular bisector vector, **H**, shown in Fig 1. D is a function of α , the angle between the angular bisector and surface normal, and a Root Mean Square (RMS) slope term, m , which parametrises the surface roughness. Higher values for m correspond to a rougher surface and hence a broader distribution in the specular reflections. Further information on the calculation of F , G and D is available in [7].

The optical characteristics of each facet of the geometry are therefore parameterised using three numbers: 1) the diffuse coefficient d , where $s = 1 - d$; 2) the RMS slope m ; 3) the diffuse albedo ω .

The final step in light curve synthesis is converting the ratio of fluxes at the i^{th} facet, B_i , to an apparent magnitude m_{app} . This is achieved by using the equation

$$m_{app} = -26.74 - 2.5 \log_{10} \left(\sum_{i=1}^{N_{facets}} \frac{B_i}{4\pi r^2} \right) \quad (4)$$

where -26.74 is the apparent magnitude of the Sun, N_{facets} is the total number of reflecting facets and r is the distance from the surface to the observer. The apparent magnitude, m_{app} , can be converted to a standard magnitude, m_{std} , by setting: $r = 1000$ km. It should be noted that the RMS slope and magnitude both use the symbol m , however magnitude will always be denoted as standard or apparent in subscript.

Position Data

The synthetic light curves in this paper were generated using real-world positions of the object, Earth and Sun, as defined by a real light curve. The real position of the object was generated using Two Line Element (TLE) data obtained from www.spacetrack.org, in conjunction with the Simple General Perturbations 4 (SGP4) orbital propagator. The real positions of the Earth and Sun were obtained from the Jet Propulsion Laboratory's HORIZONS system, available at <https://ssd.jpl.nasa.gov/?horizons>. Transformations between celestial and terrestrial coordinate systems were performed using the International Astronomical Union's (IAU) Standards Of Fundamental Astronomy (SOFA) software routines, which implement the International Earth Rotation and Reference Systems Service (IERS) 2010 conventions. This software is available from <http://www.iausofa.org/>.

Real Target Light Curve

The real target light curve selected for testing was obtained from an online database of light curves collected using the Mini-MegaTORTORA (MMT) system. The MMT system is a collection of optical telescopes owned by the Kazan Federal University and located in the Russian Caucasus. They are used to make routine observations of meteors and satellites [8]. A wide selection of MMT observations of spacecraft are available via <http://mmt.favor2.info/satellites>.

Rocket bodies at the most basic level have a common shape: cylindrical with a rocket nozzle on one end. The observed brightness of a rocket body is due to reflected sunlight from one of three zones of the object: either the end with the rocket nozzle, the end without a rocket nozzle, or the curved sides of the fuel tanks. Therefore, assuming the object is in an orientation that does not allow reflections from two of the zones simultaneously, a light curve of a tumbling rocket body would be expected to contain a repeating series of reflections at three distinct brightness levels.

Figure 2 presents six real light curves collected on a range of tumbling Low Earth Orbit (LEO) rocket bodies. In the cases that demonstrate a repeating sequence, the first four reflections from the three different zones are labelled as A, B and C. In light curves 2a, 2b and 2e this sequence of reflections is clear, whereas in 2d and 2f it is more ambiguous. Light curve 2c shows the repeating sequence, but not as clearly as is the case in light curves 2a, 2b and 2e. Two possible reasons for why this sequence is not visible in some light curves are: an orientation where two zones are reflecting simultaneously; the reflections from two or more of the zones result in similar brightness levels.

For this paper, the Long March 2D rocket body light curve in Fig. 2a was selected as the real target light curve. This light curve was also used to define the relevant position data. The properties of this light curve are given in Table 1. This light curve was selected due to the low noise and the clear repeating sequence of reflections from the three zones of the geometry.

The MMT database provides a rotational period of 9.2 s for this light curve, calculated using period folding.

Synthetic Target Light Curves

To provide a point of comparison for the real target light curve data, the rotation vector position determination technique was first applied to four synthetic target light curves for which the values of all inputs were known. To generate

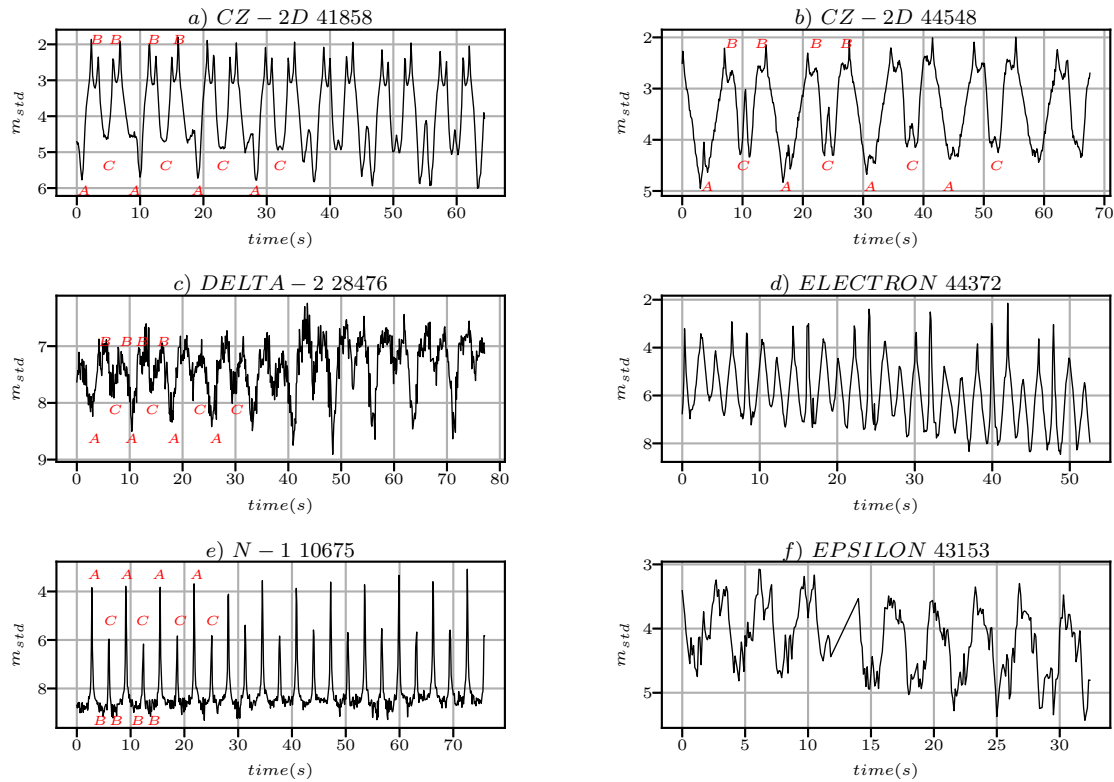


Fig. 2. Six examples of real rocket body light curves collected using MMT. Red ‘A’, ‘B’ and ‘C’ letters are used to highlight repeating sequences of reflections at three distinct brightness levels where applicable.

Tab. 1. The properties of the real target light curve.

Property	Value
Name	CZ-2D R/B
NORAD ID	41858
Start Date	11/02/17
Start Time	03:02:59
Duration	64.4 s

these synthetic light curves, some additional inputs were required: an object geometry with associated BRDF parameters for each facet; a position of the rotation vector in the body-fixed frame; the initial offset between the body-fixed and orbital reference frames.

Figure 3 shows the geometry used to generate the synthetic target light curves. This geometry is a 3.3 m by 9.5 m cylinder, capped with a cone that extends by a further 1 m from each end. The geometry was broken into three zones, with each being given individual sets of BRDF parameters. These three zones are indicated by the three colours in Fig. 3 and correspond to the top, bottom and side. The geometry was assumed to be of constant density, the center of mass is therefore the same as the geometric center.

The rotation axis in the body-fixed frame was set to be coincident with the geometry x-axis. This is a “flat spin” and is a sensible assumption for the rotation state of a tumbling rocket body [9]. The rotation angular rate was derived from the 9.2 s rotation period provided by the MMT database.

Figure 4 shows the orbital reference frame. The position of the rotation vector in this frame is given as an offset from the Earth zenith vector, using the two angles ϕ and ψ . As shown in Fig. 4, ψ is the angle between the projection of the rotation vector in the Y-Z plane and the Z-axis and ϕ is the angle between the rotation vector and the X-axis. The

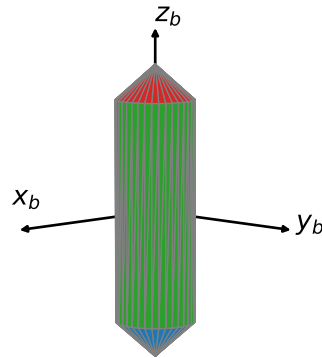


Fig. 3. Object geometry used to represent a rocket body. The red, blue and green facets indicate the three zones of the geometry which are given different reflection characteristics.

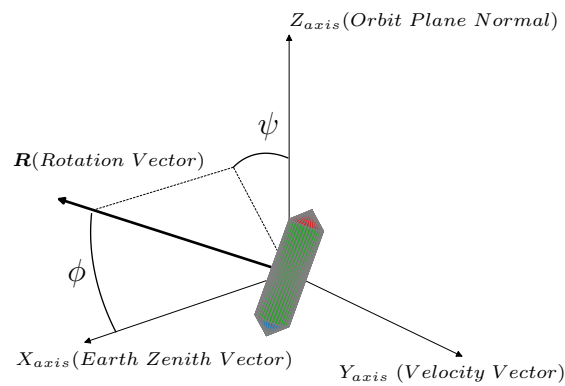


Fig. 4. The orbital reference frame used to define the position of the rotation vector. The angles ϕ and ψ describe the positions of the rotation vector with respect to the Earth zenith direction.

rotation vector is assumed to remain constant in the orbital frame. As a result of the rotation axis being aligned with the X-axis of the body-fixed frame, the position of the rotation vector in the orbital frame is the same as the offset between the orbital and body-fixed frames.

Figure 5 presents the four synthetic target light curves, generated using the randomly generated values for the BRDF parameters and rotation vector positions presented in Table 2.

Quantifying the Difference Between Two Light Curves

For this paper, the Root Mean Square Error (RMSE) was used to quantify the difference between two light curves. The RMSE is given by

$$RMSE = \sqrt{\frac{\sum_{i=1}^n (\hat{y}_i - y_i)^2}{n}}, \tag{5}$$

where n is the number of data points in the light curves, \hat{y}_i is the i^{th} value of the first light curve and y_i is the i^{th} value of the second light curve.

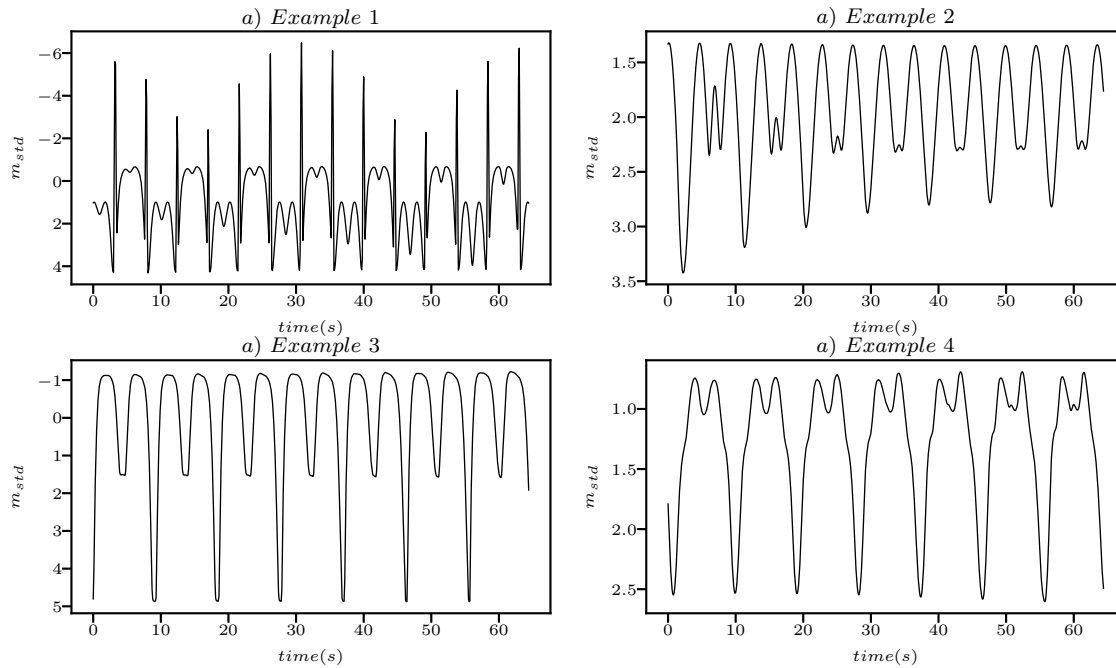


Fig. 5. Four synthetic target light curves.

Determining Best Fitting Light Curve Inputs

Next, the rotation vector position and BRDF parameters of a synthetic light curve that best fits the real target light curve was determined. This was done using the same geometry and attitude motion inputs that were used for the synthetic target light curves. The fitting was performed by manually adjusting the synthetic light curve inputs until it approximately matched the real target light curve. Then the set of best-fitting BRDF parameters were determined. To do this, only the sections of the synthetic fitting light curve that corresponded to the first reflection from the three different zones of the geometry were identified and extracted. The BRDF parameters for each of these geometry zones were then fitted individually to the corresponding sections of the real target light curve. This was achieved using a brute force method, where all combinations of the three BRDF parameters were tested using the ranges shown in Table 3. i.e [$d_{top} = 0.0, m_{top} = 0.1, \omega_{top} = 0.1$] was tested, followed by [$d_{top} = 0.0, m_{top} = 0.1, \omega_{top} = 0.2$] etc. The best-fitting set of BRDF parameters were those that minimised the RMSE between the synthetic fitting curve and the real target light curve.

Tab. 2. Table of randomly generated inputs used to generate the synthetic target light curves of Fig. 5.

Property	Generation Range	Example 1	Example 2	Example 3	Example 4
ψ	0 - 359	267	114	160	324
ϕ	0 - 90	65	15	89	9
ω_{top}	0.00 - 1.00	0.79	0.66	0.51	0.42
m_{top}	0.00 - 1.00	0.34	0.20	0.52	0.61
d_{top}	0.00 - 1.00	0.91	0.11	0.98	0.49
ω_{bottom}	0.00 - 1.00	0.77	0.08	0.73	0.63
m_{bottom}	0.00 - 1.00	0.55	0.63	0.65	0.91
d_{bottom}	0.00 - 1.00	0.26	0.65	0.84	0.09
ω_{side}	0.00 - 1.00	0.83	0.61	0.78	0.35
m_{side}	0.00 - 1.00	0.04	0.39	0.82	0.66
d_{side}	0.00 - 1.00	0.48	0.94	0.62	0.27

Tab. 3. Best-fitting inputs to fit a synthetic light curve to the real target light curve.

Property	Value	Testing Range	Step
ψ	350	0 - 350	10
ϕ	60	0 - 90	10
ω_{top}	0.20	0.1 - 0.9	0.1
m_{top}	0.80	0.1 - 0.9	0.1
d_{top}	0.40	0.0 - 1.0	0.1
ω_{bottom}	0.40	0.1 - 0.9	0.1
m_{bottom}	0.40	0.1 - 0.9	0.1
d_{bottom}	0.70	0.0 - 1.0	0.1
ω_{side}	0.20	0.1 - 0.9	0.1
m_{side}	0.40	0.1 - 0.9	0.1
d_{side}	0.60	0.0 - 1.0	0.1

3 RESULTS

The two primary results are the two polar plots in Figs. 6 and 7. Each pixel in these plots shows the RMSE, calculated using Eq. 5, between the target light curve and a new light with a rotation vector position given by the position on the polar axes. In these polar plots the radial-axis plots the angle ϕ (0° - 90°) and the theta-axis plots the angle ψ (0° - 360°). Comparing to Fig. 4, the origin of the polar plots is equal to the X-axis, the coordinate [$\phi = 90^\circ$, $\psi = 0^\circ$] corresponds to the Z-axis and the coordinate [$\phi = 90^\circ$, $\psi = 90^\circ$] is the Y-axis. The RMSE in each plot was normalised.

In Fig. 6, the RMSE was measured between the synthetic target light curves of Fig. 5 and the new light curve with a different rotation vector position. The RMSE was therefore due only to a change the rotation vector position as all other inputs remained the same. Figure 7 shows the RMSE between the real MMT target light curve and the best-fitting synthetic light curve with a range of rotation vector positions. Hence the RMSE was due to a change in the rotation vector position in addition to errors in the modelling. These included: errors in the synthetic light curve model, such as disparities in the reflection calculated by the BRDF and reality; errors in the synthetic light curve inputs, such as differences between the object geometry of Fig. 3 and the real rocket body geometry.

Figures 8 and 9 show the best-fitting synthetic light curve overlaid onto the real target light curve. Figure 8 shows only the first two full rotation periods, whereas Fig. 9 shows the full light curve.

4 DISCUSSION

Polar Plot Discussion

The four plots of Fig. 6 show the RMSE that results from only a mismatch in rotation vector position, as all other inputs remained the same. In all four plots, the real position of the rotation vector coincides with the pixel showing the lowest RMSE. This pixel shows an RMSE close to zero, as it only measures the difference that results from the 10° bins used to produce the polar plots. A number of the surrounding pixels show RMSE values within 10 - 20% of the correct solution, which is indicative of the uncertainty. The remainder of the pixels in the plot typically indicate larger RMSE values. This technique is correctly identifying the pixel that contains the rotation vector for the synthetic target light curves.

Figure 7 shows the RMSE measured between the best-fitting synthetic light curve and the real MMT target light curve, as the synthetic light curve rotation vector was varied. This plot is very similar to the results of Fig. 6: the plot contains a brightest pixel and the surrounding pixels become less bright as distance from the brightest pixel increases. However, unlike the synthetic results of Fig. 6, the inputs into the best-fitting synthetic light curve were different to their values in reality. The most substantial difference was in the object geometry. The real rocket body has a much more complex structure than the cylindrical geometry used in the synthetic light curve generation, particularly on the end with the rocket nozzle. Furthermore, the attitude state used in the synthetic light curve was simplified and the position of the rotation vector in the orbital frame was assumed to be constant. In reality the attitude motion may be

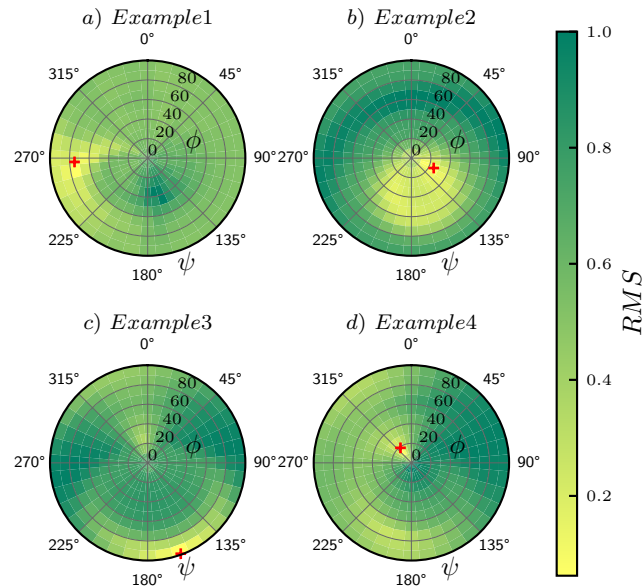


Fig. 6. The RMSE measured between the synthetic target light curves and new synthetic light curves generated with a rotation vector position given by the polar axes.

more complex. Most of these errors will be captured within the determined values for the BRDF inputs due to their use as fitting parameters.

Despite these differences between the best-fitting synthetic light curve inputs and reality, the polar plot of Fig. 7 remains similar to the synthetic polar plots for which there were no differences between inputs apart from rotation vector position. This indicates that, for this particular case, the rotation vector position determination technique is robust to errors in object geometry and BRDF modelling.

Light Curve Plot Discussion

The precise differences between the best-fitting synthetic light curve and the real MMT target light curve are shown in the final two plots, Figs. 8 and 9.

Firstly, the plot containing only the first two rotation periods, Fig. 8, is considered. A visual inspection of this figure shows a number of features which are similar between the real and synthetic light curves. These include the phase of the two curves, the positions of the peaks and troughs and the fact that the brightest reflection has two peaks, with one being slightly larger than the other. However, there are also dissimilarities between the two light curves. Most notably, in the twin-peaked brightest reflection the two curves do not precisely overlap and in the two lowest brightness reflections the shape of the synthetic curve is not the same as in the real curve. The two lowest brightness reflections in this light curve correspond to reflections from the two ends of the geometry. The ends of the geometry will have the largest differences between the geometry used in the synthetic light curve generation and reality, due to features such as a rocket nozzle not being considered. This may be the cause of the differences between the synthetic and real reflections from the ends of object.

Now considering the full light curve shown in Fig. 9. This figure additionally shows the absolute residuals with a trend line calculated using linear regression. The residuals in the plot show that the magnitude of the difference between the two curves increases with time. Because the synthetic light curve was only fit to the first rotation period of the real light curve, the residuals plot shows that the closeness of the fit slowly decreases as the light curve progresses. This indicates that there were properties, other than the viewing conditions, which were handled by the model, that changed throughout the real light curve but remained constant in the synthetic light curve. This may be, for example, because the rotation vector position does not remain constant in the orbital frame, which was one of the assumptions used in the synthetic light curve generation.

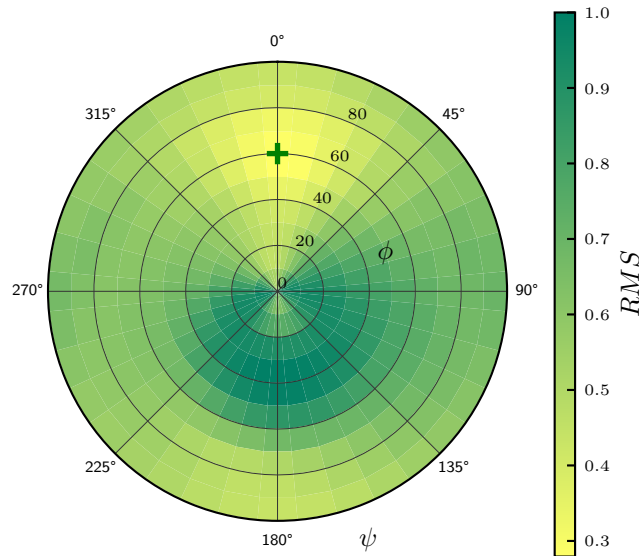


Fig. 7. The RMSE measured between the real light curve from the MMT and the best-fitting synthetic light curve generated with a new rotation vector position given by the polar axes.

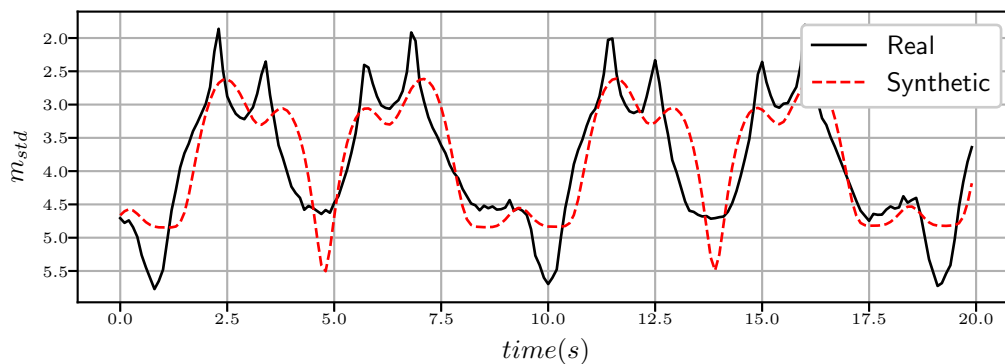


Fig. 8. Comparison between the real MMT light curve and the best-fitting synthetic light curve. This plot shows the first two rotation periods.

5 CONCLUSIONS

The results in this paper indicate that fitting a synthetic light curve to a real light curve can be used to determine the approximate position of the rotation axis, for a tumbling rocket body in a “flat spin” attitude state. In both the synthetic and real examples, varying the position of the rotation vector resulted in similar relative changes in the RMSE. This indicates that the method was not substantially affected by errors present in the object geometry and that the BRDF can be used for fitting.

Because the first steps of the fitting process were performed manually, all combinations of input parameters have not been tested. As a result, it is possible that additional best-fitting rotation vector positions exist. Furthermore, only a single real light curve was considered, which exhibited a particularly clear structure. This was required in order to facilitate the manual fitting. Although it is expected that the model would be capable of determining the rotation vector positions in light curves with less clear structure, this would need to be tested. The first steps of the future work will address these issues by automating the fitting process. This will allow a more thorough examination of the solution space in order to investigate the uniqueness of the solution. Additionally, this would allow a wider range of real rocket body light curves to be tested and confirm that this technique is applicable to rocket bodies more generally.

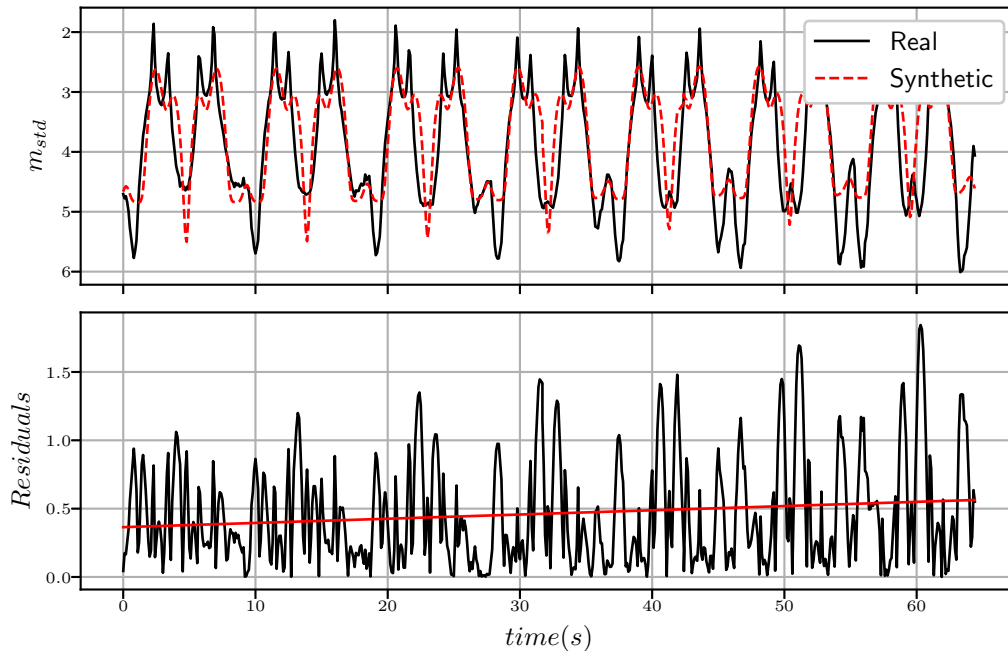


Fig. 9. Top: Comparison between the real MMT light curve and the best-fitting synthetic light curve. This plot shows the full light curve. Bottom: Absolute residuals.

References

- [1] J. C. Liou and N. L. Johnson, "A sensitivity study of the effectiveness of active debris removal in LEO," *Acta Astronautica*, vol. 64, no. 2-3, pp. 236–243, 2009.
- [2] M. Kaasalainen, J. Torppa, and K. Muinonen, "Optimization Methods for Asteroid Lightcurve Inversion II. The Complete Inverse Problem," *Icarus*, vol. 153, pp. 37–51, 2001.
- [3] J. Torppa, M. Kaasalainen, T. Michałowski, T. Kwiatkowski, A. Kryszczyńska, P. Denchev, and R. Kowalski, "Shapes and rotational properties of thirty asteroids from photometric data," *Icarus*, vol. 164, no. 2, pp. 346–383, 2003.
- [4] C. J. Wetterer and M. K. Jah, "Attitude Determination from Light Curves," *Journal of Guidance, Control, and Dynamics*, vol. 32, no. 5, pp. 1648–1651, 2009.
- [5] M. A. Earl and G. A. Wade, "Observations of the Spin-Period Variations of Inactive Box-Wing Geosynchronous Satellites," *Journal of Spacecraft and Rockets*, vol. 52, no. 3, pp. 968–977, 2015.
- [6] N. Koshkin, E. Korobeynikova, L. Shakun, S. Strakhova, and Z. H. Tang, "Remote Sensing of the EnviSat and Cbers-2B satellites rotation around the centre of mass by photometry," *Advances in Space Research*, vol. 58, no. 3, pp. 358–371, 2016.
- [7] R. Cook and K. Torrance, "A Reflectance Model for Computer Graphics," *ACM SIGGRAPH Computer Graphics*, vol. 15, no. 3, pp. 307–316, 1982.
- [8] S. Karpov, G. Beskin, A. Biryukov, S. Bondar, E. Ivanov, E. Katkova, A. Perkov, and V. Sasyuk, "MINI-MEGA-TORTORA WIDE-FIELD MONITORING SYSTEM WITH SUB-SECOND TEMPORAL RESOLUTION : FIRST YEAR OF OPERATION," *Revista Mexicana de Astronomía y Astrofísica*, no. 48, 2016.
- [9] S. Efimov, D. Pritykin, and V. Sidorenko, "Long-term attitude dynamics of space debris in Sun-synchronous orbits: Cassini cycles and chaotic stabilization," *Celestial Mechanics and Dynamical Astronomy*, vol. 130, no. 10, 2018.